fermentation

MDPI

Article

Improving the Synthesis Efficiency of Amino Acids Such as L-Lysine by Assembling Artificial Cellulosome Elements Dockerin Protein In Vivo

Nan Li [1], Le Xue [2], Zirui Wang [3], Peng Du [3], Piwu Li [3], Jing Su [3], Jing Xiao [3], Min Wang [1,*], Junqing Wang [3,*] and Ruiming Wang [3,*]

[1] College of Biotechnology, Tianjin University of Science and Technology, Tianjin 300457, China
[2] College of Life Science and Technology, Huazhong University of Science and Technology, 1037 Luoyu Road, Wuhan 430074, China
[3] State Key Laboratory of Biobased Material and Green Papermaking (LBMP), Qilu University of Technology, Jinan 250353, China
* Correspondence: minw@tust.edu.cn (M.W.); wjqtt.6082@163.com (J.W.); ruiming3k@163.com (R.W.)

Abstract: Cellulosome is a highly efficient multi-enzyme self-assembly system and is found on the extracellular surface or in the free environment of microorganisms. However, with a lack of Ca^{2+} in vivo, cellulosome assembly is challenging. In this study, a novel design method was used to directionally modify the Ca^{2+}-binding site, and four double-site dockerin A (DocA) mutants were obtained. At a Ca^{2+} concentration between 1.00×10^{-7} and 1.00×10^{-4} M, the mutant DocA-D3 had the strongest binding capacity to cohesion (Coh), which was 8.01 times that of DocA. The fluorescence signal intensity of the fusion proteins assembled using mutants was up to 1.26×10^{7} in *Escherichia coli*, which indicated that these mutants could interact with Coh in vivo. The molecular dynamics simulation results showed that DocA-D3 could maintain a stable angle structure without Ca^{2+}, and when applied to L-lysine fermentation, the yield was increased by 24.1%; when applied to β-alanine fermentation, the product accumulation was increased by 2.13–2.63 times. These findings lay the foundation for assembly design in cells.

Keywords: cellulosome; self-assembly; in vivo; Ca^{2+} concentration; rational design method

check for updates

Citation: Li, N.; Xue, L.; Wang, Z.; Du, P.; Li, P.; Su, J.; Xiao, J.; Wang, M.; Wang, J.; Wang, R. Improving the Synthesis Efficiency of Amino Acids Such as L-Lysine by Assembling Artificial Cellulosome Elements Dockerin Protein In Vivo. *Fermentation* **2022**, *8*, 578. https://doi.org/10.3390/fermentation8110578

Academic Editor: Xiaoqing Hu

Received: 8 September 2022
Accepted: 20 October 2022
Published: 25 October 2022

1. Introduction

L-lysine is currently mainly used in the feed industry to supplement the missing L-lysine components in animal feed, which can effectively improve the utilization of protein components in feed, save costs, and reduce pollution. In addition to the application of L-lysine in the feed industry, it is also widely used in food, medicine, and other industries, and has important application value. Further increasing the fermentation intensity of L-lysine has been an important direction for the breeding of L-lysine industrial production strains in recent years.

Recent studies have found that the cascade of biocatalytic reactions can lead to complex, efficient, and selective intracellular transformation [1]. Using multi-enzyme fusion, self-assembly, and other methods to construct a multi-enzyme complex in the cell, the transfer and processing distance of intermediate metabolites between the catalytic active centers of different enzymes can be shortened [2–4]. In addition, the catalytic rate of each enzyme can indirectly increase, thereby improving the product synthesis efficiency [5]. By introducing exogenous gene modules into the chassis cells to achieve new functions, an effective multi-enzyme assembly system can be provided, thereby improving its synergistic catalytic function, which is conducive to the regionalized design of multi-enzyme catalysis in synthetic biology.

A natural multi-enzyme complex, cellulosome, has been discovered in various anaerobic microorganisms [6]. Compared with other bacterial intracellular multi-enzyme complex

systems, cellulosomes have the advantages of a small molecular weight, their scaffoldins have multiple binding sites, they are rich in dockerin (Doc) types of proteins, and they have strong designability. Research has shown that the efficient degradation of different substrates by cellulosomes requires different enzyme compositions, and the diversity of cellulases is equally important, so different cellulosome structures are also required [7]. Cellulosomes are mainly composed of two parts: Doc proteins containing enzymes or other auxiliary proteins and cohesin (Coh)-containing structural proteins. The latter are also called scaffolding proteins (Sca). Each enzyme of the cellulosome has a single dockerin module and at least one non-enzyme scaffolding component. Cellulosome formation by *Clostridium thermocellum* is mediated by two specific interactions: one interaction is between the type-I dockerin module at the C-terminus of cellulosomal components and the internal nine type-I cohesin modules of the primary scaffoldin protein, CipA, and the other is mediated between the type-II dockerin module at the C-terminus of CipA and the internal type-II cohesin modules of the cell-surface-displayed and unbound secondary scaffoldin proteins. The cellulosome in *C. thermocellum* is the most widely studied and the most typical cellulosome model. It mainly consists of three parts: the enzyme-containing type I Doc protein, the primary scaffold protein, and the anchor scaffold protein [8]. Cellulosomes have been successfully displayed on the extracellular surface of bacteria, yeast, and other microorganisms as a natural and highly efficient multi-enzyme self-assembly system [9–11]. At the same time, they provide a new idea for the intracellular self-assembly of multiple enzymes.

Doc and Coh proteins are key elements in cellulosomes in *C. thermocellum*. Doc is a protein module without a catalytic function in the enzyme complex and is generally composed of about 70 amino acid residues, which contain two roughly repeated fragments, each fragment containing about 22 amino acid residues [12,13]. Doc proteins can specifically bind to Coh, that is, type I Doc proteins can only bind to type I Coh and one Doc protein can only bind to one Coh; the structure does not change before and after binding. Both the formation of a stable Doc protein structure and the binding of Doc and Coh require the participation of Ca^{2+}. One Ca^{2+}-binding site is close to the N-terminus, and the other Ca^{2+}-binding site can stabilize the connection of the loop region [14].

For anaerobic bacteria, Ca^{2+} plays an important role in the structural stability and functional integrity of Doc proteins. Previous studies have found that after chelating Ca^{2+} with EDTA, the Doc of anaerobic bacteria can no longer interact with Coh [15,16]. The interaction between extracellular Doc and Coh for efficient self-assembly requires the presence of Ca^{2+} at a certain concentration ($0.50–2.00 \times 10^{-3}$ M) [17,18]. However, due to the strict control of components, such as Ca^{2+} channels [19], Ca^{2+} concentration in microbial cells at rest is generally only 1.00×10^{-7} M, which is much lower than the extracellular concentration (1.00×10^{-3} M). This limits the interaction and self-assembly of Doc and Coh in the cell.

In this study, to resolve the problem of strong extracellular Ca^{2+} dependency in Doc and Coh protein assembly, the Ca^{2+}-binding region of Doc was studied. Doc mutants that do not depend on Ca^{2+} were designed. The self-assembly of the key components of cellulosomes without Ca^{2+} dependency was achieved, thus solving the problem of intracellular self-assembly of Doc and Coh. This laid the foundation for the successful construction of an intracellular self-assembly system based on the cellulosome as a model.

2. Materials and Methods

2.1. Strains and Media

E. coli BL21(DE3), as an expression host, was cultured in Luria Broth (LB) medium at 37 °C. The pET-28a(+) and pETDuet-1 vectors (Sangon, Shanghai, China) were used for gene cloning. The enzymes used for DNA amplification and restriction and the plasmid extraction kit were obtained from Vazyme (Nanjing, China). The primers were synthesized by Qingke (Beijing, China). The partial molecular fragments applied to bimolecular fluorescence complementation coupled with flow cytometry (BiFC-FC) were synthesized using

GenScript (Nanjing, China). All chemicals were purchased from Sigma-Aldrich (St. Louis, MO, USA). The strains and plasmids used are shown in Table 1.

Table 1. List of strains and plasmids used in this study.

Strains/Plasmids	Relevant Genotype	Source
Strains		
E. coli DH5α	Amplification and extraction of plasmids	Vazyme
E. coli BL21(DE3)	Protein expression and extraction	Vazyme
E. coli QDE	L-lysine fermentation; Δ*ldcC*, Δ*amiD*, Δ*LYP1*, *icd*-D410E, *pykA*-G168D	This study
Plasmids		
pET-28a(+)-DocA	Expression of dockerin protein DocA	This study
pET-28a(+)-Coh	Expression of adhesin protein Coh	This study
pET-28a(+)-DocA-D1	Expression of protein DocA-D1	This study
pET-28a(+)-DocA-D2	Expression of protein DocA-D2	This study
pET-28a(+)-DocA-D3	Expression of protein DocA-D3	This study
pET-28a(+)-DocA-D4	Expression of protein DocA-D4	This study
pETDuet-1-eYFP(N)-Coh/DocA-eYFP(C)	BiFC expression protein DocA	This study
pETDuet-1-eYFP(N)-Coh/DocA-D1-eYFP(C)	BiFC expression protein DocA-D1	This study
pETDuet-1-eYFP(N)-Coh/DocA-D2-eYFP(C)	BiFC expression protein DocA-D2	This study
pETDuet-1-eYFP(N)-Coh/DocA-D3-eYFP(C)	BiFC expression protein DocA-D3	This study
pETDuet-1-eYFP(N)-Coh/DocA-D4-eYFP(C)	BiFC expression protein DocA-D4	This study
pETDuet-1-eYFP(N)-Scat/Stag-eYFP(C)	BiFC expression protein SpyCatcher/SpyTag	This study
pETDuet-1-aspC-Coh/DocA-D3-lysC	Intracellular assembly fermented L-lysine	This study

The genes corresponding to Coh and DocA were codon-optimized according to the *E. coli* BL21(DE3) genome and synthesized using GenScript (Nanjing, China). The pET-28a(+) plasmid with an inducible T7 promoter was used for heterologous expression of Coh and DocA with a His-Tag. The construction process and the schematic diagram of the recombinant plasmid are shown in Figure S1. The obtained pET-28a(+)-Coh and pET-28a(+)-DocA vectors were transformed into *E. coli* BL21(DE3) via electroporation.

2.2. Selection of Key Components of Cellulosomes

The research model of the intracellular self-assembly system was the natural multi-enzyme complex, i.e., the cellulosome. The focus was on the study of the intracellular assembly of Doc and Coh. Using the National Center for Biotechnology Information (NCBI; https://blast.ncbi.nlm.nih.gov/Blast.cgi, accessed on 6 March 2021) and Protein Data Bank (PDB; http://www.rcsb.org, accessed on 6 March 2021) databases, we downloaded the amino acid sequence and crystal structure, and then preliminary analysis was performed using PyMOL 2.3.2 software. DocA (PDB DOI: 10.2210/pdb2CCL/pdb; ID: 2CCL-B) [20] and Coh (PDB DOI: 10.2210/pdb1OHZ/pdb; ID: 1OHZ) [14] with the existing crystal structure as the original intracellular self-assembly system were selected. Both proteins were derived from *C. thermocellum*.

2.3. Expression and Purification of DocA and Coh

The verified strain was first cultured overnight in 50 mL of liquid LB medium containing kanamycin (50 μg/mL) and then inoculated into fresh liquid LB medium at 1% inoculum. After culturing for 10 h, when the culture reached an optical density of 1.0 at 600 nm (OD600), isopropyl β-D-1-thiogalactopyranoside (IPTG) was added to a final concentration of 0.2 mmol/L at 22 °C for protein induction. After collecting the induced bacterial cells, we resuspended them in 2× phosphate-buffered saline (PBS) buffer, added an appropriate amount of protease inhibitors, and broke them down using an ultrasonic disintegrator (Scientz-650E, Xinzhi, Ningbo, China). A cobalt column with higher specificity was used for protein purification, and the entire operation was performed in a 4 °C chromatography cabinet.

The purified protein was detected via sodium dodecyl sulfate-polyacrylamide gel electrophoresis (SDS-PAGE) and the protein purity was ascertained. The proteins that met the requirements were collected, and desalting/concentration treatments were separately performed. DocA was dialyzed to remove salt using PBS-EP$^+$ buffer, and Coh was dialyzed to remove salt using acetic acid–sodium acetate buffer at different pH values (pH 3.6–4.6).

2.4. Mutation and Verification of DocA

Molecular dynamics (MD) simulation and molecular biology were used in combination to mutate DocA. Mutation points were selected using PyMOL 2.3.2. Amino acids within 4 Å from the Ca^{2+} in the Ca^{2+}-binding site of DocA were selected as key amino acids for Ca^{2+} binding.

For the two key Ca^{2+}-binding sections, $D^5VN^7GD^9GTINSTD^{16}$ and $D^{39}VD^{41}KN^{43}GSINAAD^{50}$, there were 16 possibilities in total, with Thr and Ser having similar hydrophilic side chains but uncharged and hydrophobic amino acids that facilitated folding. Based on this, the combination of Ca^{2+} and key amino acids was designed for mutation primers, and the protein sequence was submitted to the Rosetta website (http://rosettadesign.med.unc.edu/register.php, accessed on 12 March 2021) for protein structure prediction, protein-protein docking, and protein design; four double-site DocA mutants were obtained. Based on the calculation, the amino acid sequence was optimized according to the *E. coli* expression system, and a combination of mutant primers with Ca^{2+} and key amino acids was designed (forward and reverse primers, respectively, covered the two Ca^{2+}-binding sites of DocA). The primer sequences used for the mutant amino acids are shown in Table 2, and the verification primers are shown in Table S1. Rapid site-directed mutagenesis was used to obtain the mutants.

Table 2. The list of double-site mutation primers used in this study.

Protein	Primer Name	Sequence (5′→3′)
DocA-D1	D1-F1	TGGGTGACGTG tct GGTGACGGT cgt ATTAATA
	D1-R1	AGATCGGTGCTATTAAT acg ACCGTCACC aga CAC
	D1-F2	AAAGCCCGTGCCGAT accagcaat AATGGC acc ATTAATG
	D1-R2	AGAACATCGGCGGCATTAAT ggt GCCATT attgctggt ATCG
DocA-D2	D2-F1	AATGGT agc GGTACCATTAATAGCA
	D2-R1	TACC gct ACCATTCACGTCACCCAGCA
	D2-F2	CGAT accagcaat AATGGC acc ATTAATGCCGCCGATGTTCT
	D2-R2	ATTAAT ggt GCCATT attgctggt ATCGGCACGGGCTTTGGCA
DocA-D3	D3-F1	GTG gat GGT agc GGT cgt ATTAATAGCACCGAT
	D3-R1	TTAAT acg ACC gct ACC atc CACGTCACCCAGCA
	D3-F2	CGAT accagcaat AATGGC acc ATTAATGCCGCCGATGTTCT
	D3-R2	ATTAAT ggt GCCATT attgctggt ATCGGCACGGGCTTTGGCA
DocA-D4	D4-F1	AATGGT agc GGTACCATTAATAGCA
	D4-R1	GTACC gct ACCATTCACGTCACCCAG
	D4-F2	ATGTG agc AAA gat GGCAGCATTAATGCCGCCGAT
	D4-R2	TGCC atc TTT gct CACATCGGCACGGGCTTTGGCA

Note: lowercase letters are mutation sites.

2.5. Detection of DocA and Coh Binding

Using the Biacore T200 molecular interaction analyzer to explore the binding mechanism of DocA and Coh, Coh was anchored on a suitable chip, and DocA mixed with different concentrations of $CaCl_2$ was allowed to flow through [21].

Next, we gradually diluted the acetic acid–sodium acetate buffers at different pH values according to the approximate protein concentration. As the proteins had to be anchored, the optimal anchoring concentration and pH were determined according to the anchoring situation, and then protein anchoring was performed using the capture method in the *Biacore Small Molecule Application Manual*.

Using standard protocols, the purified Coh was immobilized on the entire surface of a CM5 sensor, and the anchored chip was loaded into the analyzer. The channel containing the DocA mutant sample was set as the detection channel and that of the original DocA

as the reference channel. 4-(2-Hydroxyethyl)-1-piperazineethanesulfonic acid (HEPES)-buffered saline was used as the mobile phase, the flow rate of the flow pool was 10 μL/min, the temperature ranged between 20 °C and 23 °C, and the pH ranged between 7.0 and 7.4. DocA was diluted to almost the same concentration as the Coh anchor, and $CaCl_2$ was serially diluted to 1.00×10^{-2}, 1.00×10^{-3}, 1.00×10^{-4}, 1.00×10^{-5}, 1.00×10^{-6}, and 1.00×10^{-7} M, and placed at 4 °C for at least 30 min for detection. Each experiment for each concentration was performed in triplicate. After centrifugation, the ligand was injected into the detection and reference channels at the rate of 10 μL/min and the binding status was determined according to the AbsResp value. The kinetic/affinity method in Bicaore T200 was used to analyze the interaction between ligand and receptor.

2.6. BiFC-FC

BiFC-FC was used to verify the effects of the interaction of different Doc mutants and Coh in vivo. The enhanced yellow fluorescent protein (eYFP) was chosen and divided into two fragments: eYFP-N (1–155) and eYFP-C (156–238). These two fragments were then connected to DocA and Coh, respectively, with a longer connecting peptide SGGGSGGGSGGS. The N-terminal (such as Gly-5) of Coh was closer to the N- and C-terminal of DocA. The C-terminal (Ile-59) of DocA has no calcium-binding site; therefore, we selected the N-terminal of Coh and the C-terminal of DocA for eYFP fusion. After ligation, it was simultaneously expressed on the dual-promoter expression plasmid pETDuet-1 (see Figure S1), and the transformation was verified. The verification primers are shown in Table S1. If there was an interaction between the DocA mutant and Coh, the N- and C-terminal fragments of the fluorescent protein were drawn close to each other through the linker, forming a fluorescent protein chromophore to re-fluorescence. The MoFlo XDP system of the flow cytometer with an Xcess control panel was selected for FC analysis, and a 488 nm blue laser was selected as the excitation wavelength. The application of FC technology to quantitatively analyze the BiFC signal in a single cell has become a standard method for living-cell BiFC experiments [22–24].

2.7. MD Simulation

The molecular docking software Rostta DOCK 3.4 was used to construct the DocA–Coh complex. MD simulation was performed using Gromacs 4.5.4 with a GROMOS 96 force field and an SPC/E explicit water model. Each system was minimized and equilibrated until the maximum force reached 10 kJ/mol/nm, as previously described [25]. Then, we gradually equilibrated the equilibration systems at 300 K for 100 ps with the restrained protein and ligands. After applying periodic boundary conditions, electrostatic interactions were treated using the Particle Mesh Ewald method. The integration step was set to 0.002 ps, and bonds were constrained using the LINCS algorithm. After the first equilibration, a 10 ns full equilibration was adopted without restraint, and then the g_rms tool was used to analyze the root-mean-square deviation (RMSD) values of the interacting enzymes.

2.8. Assembly and Detection of Key Enzymes in L-Lysine Fermentation

The key components of cellulosomes, DocA-D3 and Coh, were connected to the key enzymes of L-lysine fermentation aspartate aminotransferase (AspC) and aspartate kinase (LysC) in *E. coli* through the linking peptide SGGGSGGGSGGS, respectively, and were cloned into the pETDuet-1 plasmid for co-expression (see Figure S1). Then, the recombinant plasmid was transferred to the L-lysine-producing *E. coli* QDE to obtain *E. coli* QDE-DocA-D3 engineering bacteria. The bacteria were inoculated into 50 mL of seed culture medium and cultured at 37 °C and 220 r/min for 16 h as the seed solution. The seed liquid was inoculated into a 5 L fermenter at 15% inoculum [26]. The filling volume was 3 L. Fermentation conditions were as follows: 37 °C; pH 6.7; 300 r/min; glucose concentration = 2.0%; dissolved oxygen = 20–35%; and 25% ammonia water in a continuous flow. After induction, the fermentation time was less than 40 h with sampling and testing every 4 h. The concentration of bacterial cells was determined

using an ultraviolet spectrophotometer (UV-6100, METASH, Shanghai, China) to detect the absorbance of the sample at 600 nm after dilution. The glucose and L-lysine content were measured using a biosensor (BSA-90, Jinan Yanke Co., Ltd., Jinan, China).

2.9. Assembly and Detection of Key Enzymes in β-Alanine Fermentation

DocA-D3 and Coh were linked to two key enzymes of β-alanine fermentation in *E. coli*, L-aspartase (AspA), and L-aspartate α-decarboxylase (PanD), respectively, through the linker peptide SGGGSGGGSGGS and cloned into the co-expression plasmid pETDuet-1. Then, the recombinant plasmid was transferred into *E. coli* QD01 to obtain *E. coli* QD01-DocA-D3-Ala engineered bacteria. The strains were inoculated into 50 mL of seed medium, cultured at 37 °C at 220 r/min until an OD600 of 1.0, induced with IPTG at a final concentration of 0.2 mmol/L, and placed at 28 °C to allow expression for 15 h. Then, 50 mL of bacterial liquid was collected via centrifugation, resuspended in buffer, and adjusted to pH 7.0. Sodium glutamate (10 g/L) and oxaloacetic acid (10 g/L) were added, and the culture was placed in a constant-temperature water bath shaker at 37 °C, 200 rpm, with samples taken every 2 h.

β-alanine was detected via pre-column derivatization with 2,4-dinitrofluorobenzene (DNFB). Exactly 100 μL of the sample was taken and 100 μL of 0.5 mol/L sodium bicarbonate solution (PH9.0), as well as 100 μL of 1% 2,4-dinitrofluorobenzeneacetonitrile, were added. The sample was mixed well and placed in a water bath at 60 °C for 1 h in the dark. After cooling at 20–25 °C, 700 μL of 0.05 mol/L phosphate buffer (pH 7.0) was added; the supernatant was collected via centrifugation, filtered through a 0.22 μm microporous membrane, and then injected for analysis.

Mobile phase A was sodium acetate (2.5 g/L sodium acetate, 1.5 mL acetic acid, made up to 1 L with ultrapure water); mobile phase B was pure methanol. Liquid chromatography conditions were as follows: A:B = 1:1, flow rate = 1 mL/min, C18 column temperature was 40 °C, the injection volume was 10 μL, UV wavelength was 360 nm, and the detection time was 20 min.

3. Results and Discussion

3.1. Selection of the Self-Assembly System

In order to improve the efficiency of intracellular catalytic synthesis, we focused on the formation mechanism of the bacterial intracellular multienzyme complexes. Research on the formation of a bacterial intracellular multi-enzyme complex system has mainly focused on the multi-enzyme complex in the bacterial microcompartment and artificial self-assembled proteins [27–29]. Rae and Kerfeld et al. found two types of capsid proteins, α and β, that could form a spherical carboxylase body in *Cyanobacteria*. With the help of the carboxylase body, different assembly methods were used to combine carbonic anhydrase and ribulose-1,5-bisphosphate carboxylase/oxygenase, which was encapsulated in it and assembled into a multi-enzyme complex [30,31]. Similarly, the SpyTag/SpyCatcher system derived from the CnaB2 domain has usually been used for the assembly between two proteins by forming a stable isopeptide bond [32–34] and has been widely used in biological coupling, vaccine synthesis, and heat-resistant enzyme preparation [35–38]. However, as most synthetic pathways are considered relatively lengthy, especially in synthetic biology [39–41], a more concise and efficient intracellular self-assembly system for complex enzymes is still lacking [42,43].

However, when learning the ways to achieve extracellular assembly of cellulosome, things appear to have changed. This structure allows for different enzymes to be assembled by scaffolding proteins in a certain proportion to flexibly regulate the types of enzyme proteins and improve the catalytic efficiency of enzymes [44]. The efficiency of cellulosomes to hydrolyze cellulose is six times that of free enzymes [45–47]. Cellulosome is used to self-assemble multiple enzymes that degrade lignocellulose on the extracellular surface. It gives full play to the proximity effect between the assembled enzymes, improving lignocellulose-hydrolytic efficiency [48]. Cellulosomes are also used in biomass degradation, ethanol

and 2,3-butanediol synthesis [49], and biosensors; other fields, too, have realized the applications of cellulosomes [50–53].

3.2. Selection and Expression of Key Components of Cellulosomes

To evaluate the self-assembly properties of cellulosome elements in cells, the DocA [20] and Coh [14] from the existing crystal structure pool were selected as two typical cellulosome elements for self-assembly analysis. Both proteins were derived from *C. thermocellum*, which has been studied in depth and can interact stably. After IPTG-induced heterologous expression and purification, Coh and DocA were obtained and detected via SDS-PAGE. The size of Coh was 16 KDa, and that of DocA was 7 KDa (Figure S2).

However, because of metabolic needs, the Ca^{2+} concentration in microbial cells is much lower than the extracellular concentration, limiting the self-assembly of cellulosomes and their components in the cell. The concentration of Ca^{2+} affects the self-assembly of cellulosomes [54].

In this study, the binding affinities of Coh and DocA were measured on the Biacore T200 molecular interaction system (GE Healthcare, Chicago, IL, USA). The results showed that stable binding of unmutated DocA (Figure 1A,B) and Coh required a certain Ca^{2+} concentration (Figure 2C). When the Ca^{2+} concentration was 5.00×10^{-3}–1.00×10^{-2} M, the binding capacity of the two proteins decreased with an increase in the Ca^{2+} concentration; the higher the Ca^{2+} concentration, the more unstable the measured data. When the concentration was less than 1.00×10^{-4} M, the binding capacity of the two proteins was close to the binding capacity without Ca^{2+}. Therefore, preliminarily, the Ca^{2+} concentration required for Doc and Coh to form a stable structure was 5.00×10^{-3} M. The electrostatic interactions in the calcium-binding pocket may modulate the mechanostability of the cellulose-binding module [55]. MD simulation in explicit water was also performed to study the stability of DocA (with or without Ca^{2+}) under a GROMOS 96 force field (protein portion) and SPC/E (water model) using Gromacs 4.5.4 [56]. The detailed analysis and comparison of MD simulation results showed that the RMSD was 0.18 with Ca^{2+} and 0.36 when the DocA lacked Ca^{2+}.

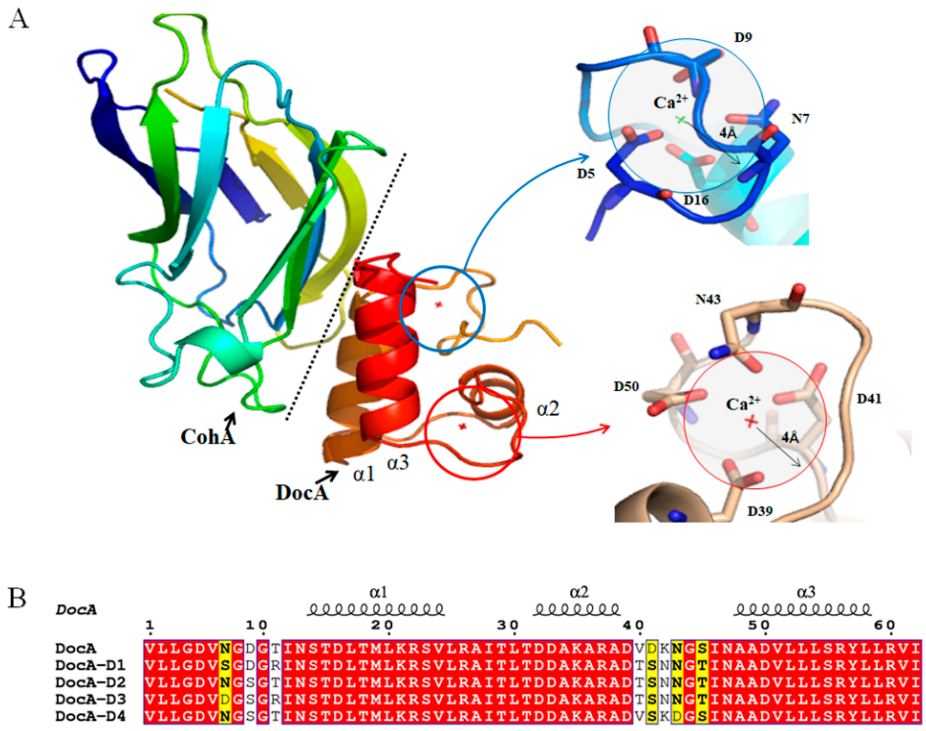

Figure 1. Coh and DocA mutation strategy. (**A**) The structure of the Coh–DocA complex and the mutation design of Ca^{2+} binding key amino acid. (**B**) Alignment of protein sequence of docking protein DocA mutants.

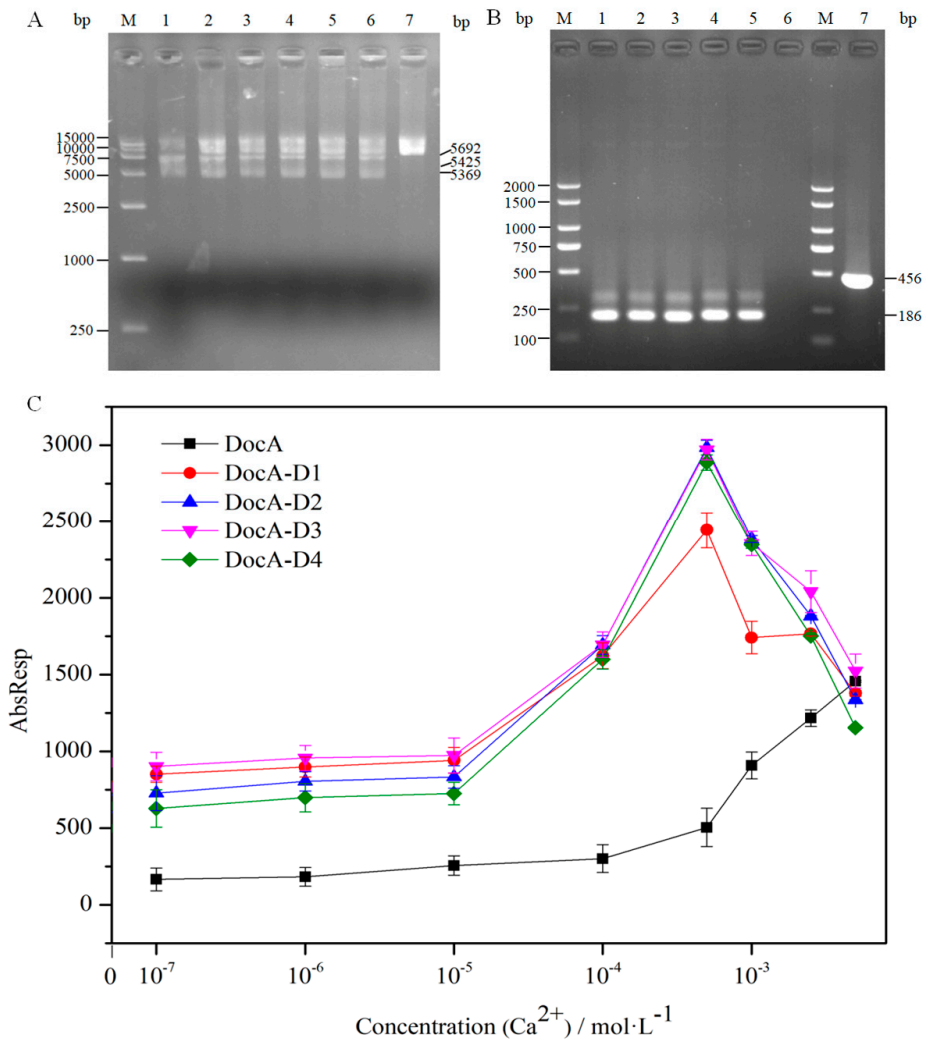

Figure 2. In vitro verification of the binding of DocA mutants to Coh. (**A**) Validation of recombinant plasmids for mutant proteins. M: marker DL15000; 1: 5369 bp DNA of pET-28a(+); 2: 5425 bp DNA of pET-28a(+)-DocA; 3: 5425 bp DNA of pET-28a(+)-DocA-D1; 4: 5425 bp DNA of pET-28a(+)-DocA-D2; 5: 5425 bp DNA of pET-28a(+)-DocA-D3; 6: 5425 bp DNA of pET-28a(+)-DocA-D4; 7: 5692 bp DNA of pET-28a(+)-Coh. (**B**) Verification of the mutant proteins engineering strains. PCR product of the mutant gene. M: marker DL2000; 1: 186 bp DNA fragment of DocA gene; 2: 186 bp DNA fragment of DocA-D1 gene; 3: 186 bp DNA fragment of DocA-D2 gene; 4: 186 bp DNA fragment of DocA-D3 gene; 5: 186 bp DNA fragment of DocA-D4 gene; 7: 456 bp DNA fragment of Coh gene. (**C**) Changes in the binding of DocA mutants and Coh under different Ca^{2+} concentrations.

3.3. Mutation of Coh and DocA

Using MD simulation and 3D structure analysis, we found that Ca^{2+} maintained the stability of the loop region in DocA, the key element of cellulosomes, and ensured that the double α-helix was connected to the loop region. DocA can interact with Coh at a certain angle for the autonomous assembly of cellulosomes. There are two Ca^{2+}-binding sites for Doc, one of which is used to stabilize its structure and the other for stable binding to Coh [14,20]. Based on this, the Ca^{2+}-binding site of DocA was designed. After analyzing the 3D structure of the Coh–DocA complex using PyMOL 2.3.2, eight amino acids within 4 Å of Ca^{2+} in the Ca^{2+}-binding site of DocA were selected as the potential target (Figure 1A). A 3D structure of DocA without Ca^{2+} was constructed using PyMOL 2.3.2 and then submitted to the Rosetta website (http://rosettadesi gn.med.unc.edu, accessed on 12 March 2021) for stable protein structure prediction. After the prediction, the four most stable double-site DocA mutants without Ca^{2+} (DocA-D1, DocA-D2, DocA-D3, and

DocA-D4) were obtained. The protein sequence alignment is shown in Figure 1B. After using site-directed mutagenesis technology to complete the mutants as predicted, the heterologous expression vectors of DocA-D1, DocA-D2, DocA-D3, and DocA-D4 were successfully constructed and expressed in *E. coli* BL21(DE3). The construction verification of mutant protein engineering strains is shown in Figure 2A,B. The mutants were also purified using affinity chromatography.

3.4. In Vitro Verification of DocA Mutant Binding to Coh

The binding of the four successfully expressed DocA double-site mutants and Coh was tested at different Ca^{2+} concentrations. Then, the corresponding AbsResp value was obtained using the Biacore T200 molecular interaction analyzer (GE Healthcare). From the data analysis shown in Figure 2C, when the Ca^{2+} concentration was 1.00×10^{-7}–1.00×10^{-3} M, the binding of the mutants to Coh greatly improved. When the lowest Ca^{2+} concentration was 1.00×10^{-7} M, the binding capacity of the mutants to Coh was in the following decreasing order: DocA-D3 > DocA-D1 > DocA-D2 > DocA-D4. The binding capacity was 8.01, 7.32, 6.25, and 5.41 times higher, respectively, compared to wild-type DocA binding to Coh. When the Ca^{2+} concentration was 1.00×10^{-7}–1.00×10^{-4} M, the binding capacity of the mutants to Coh was in the following decreasing order: DocA-D3 > DocA-D1 > DocA-D2 > DocA-D4. When the Ca^{2+} concentration was 1.00×10^{-7}–1.00×10^{-5} M, the binding of the mutants to Coh did not change much with the change in Ca^{2+} concentration. The gap between DocA and Coh remained stable. When the Ca^{2+} concentration was 1.00×10^{-5}–1.00×10^{-4} M, the binding of the four mutants to Coh began to significantly increase with an increase in the Ca^{2+} concentration. When the Ca^{2+} concentration was 10^{-4} M, the binding of the four mutants to Coh was the same, i.e., 5.5 times that of wild-type DocA. When the Ca^{2+} concentration was 5.00×10^{-4} M, the binding of the mutants to Coh was the strongest, with DocA-D3 and DocA-D2 having the best binding affinity, i.e., 5.9 times that of DocA. The binding affinity of DocA-D4 to Coh was slightly worse than that of DocA-D3 and DocA-D2 to Coh, which was 5.71 times that of DocA. DocA-D1 was weaker, with a binding affinity 4.83 times that of DocA. When the Ca^{2+} concentration was 1.00×10^{-3}–5.00×10^{-3} M, the binding of the four mutants to Coh was first enhanced and then weakened compared with DocA. When the Ca^{2+} concentration was 5.00×10^{-3} M, the binding capacity of the mutants to Coh, except for DocA-D3, was lower than that of DocA (Figure 2C). The higher the Ca^{2+} concentration, the larger the standard deviation of the AbsResp value representing the binding capacity. In summary, all the double-site mutants could interact with Coh at low Ca^{2+} concentrations; however, the binding affinity of DocA-D3 was higher than that of other mutations.

3.5. In Vivo Verification of DocA Mutant Binding to Coh

To further analyze the assembly of the mutants and Coh in cells, BiFC-FC was used. Then, the real-time detection of the protein–protein interaction of DocA mutants and Coh in the cell was performed. To verify the interaction of different DocA mutants and Coh in vivo, eYFP was selected for BiFC-FC analysis. eYFP was divided into two fragments, eYFP(N) and eYFP(C), which were, respectively, connected to the DocA mutant and Coh through a connecting peptide (SGGGSGGGSGGS). The fusion proteins were heterologously expressed in *E. coli* BL21(DE3) and verified via fermentation; simultaneously, the interaction peptide pair SpyCatcher/SpyTag-fusion proteins were designed for comparative analysis. The verification of the fusion proteins used in BiFC-FC is shown in Figure 3A,B. Using a flow cytometer, the number of positive cells and the average fluorescence intensity of the fluorescent signal could be quantitatively analyzed. As shown in Figure 3C,D, the fluorescence intensities of DocA-D1, DocA-D2, DocA-D3, and DocA-D4 were 1.22×10^7, 1.26×10^7, 1.03×10^7, and 8.32×10^6 (the fluorescence intensity of DocA being 1.00×10^6), respectively. These results indicated that DocA-D1, DocA-D2, and DocA-D3 had a significantly improved ability to bind to the Coh in cells. Considering that DocA mutants and Coh are mainly bonded via hydrogen bonds, the bonding strength was less than that of SpyCatcher/SpyTag composed of isopeptide bonds (Figure 3C).

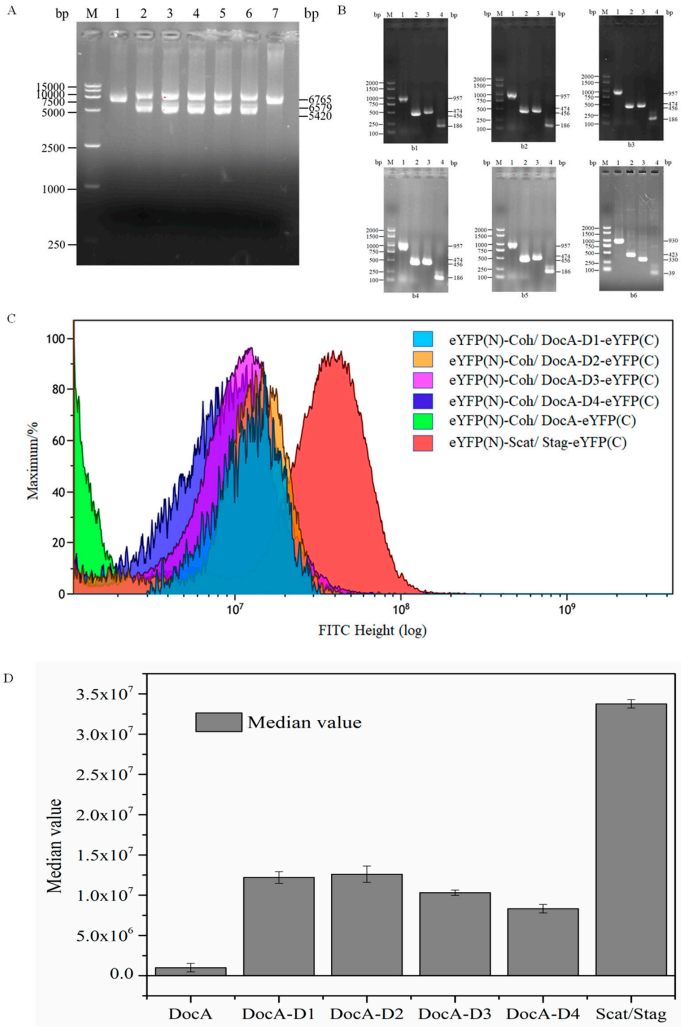

Figure 3. In vivo fluorescence verification of the binding of DocA mutants to Coh. (**A**) Verification of the recombinant plasmids for the fusion protein eYFP-DocA mutants/Coh. M: marker DL15000; 1: 5420 bp DNA of pETDuet-1; 2: 6765 bp DNA of pETDuet-1-eYFP(N)-Coh/DocA-eYFP(C); 3: 6765 bp DNA of pETDuet-1-eYFP(N)-Coh/DocA-D1-eYFP(C); 4: 6765 bp DNA of pETDuet-1-eYFP(N)-Coh/DocA-D2-eYFP(C); 5: 6765 bp DNA of pETDuet-1-eYFP(N)-Coh/DocA-D3-eYFP(C); 6: 6765 bp DNA of pETDuet-1-eYFP(N)-Coh/DocA-D4-eYFP(C); 7: 6579 bp DNA of pETDuet-1-eYFP(N)-SpyCatcher/SpyTag-eYFP(C). (**B**) Verification of the mutant protein engineering strains. PCR product of the mutant gene. (b1) M: marker DL2000; 1: 957 bp DNA fragment of fusion eYFP(N)-Coh gene; 2: 456 bp DNA fragment of Coh gene; 3: 474 bp DNA fragment of fusion DocA-eYFP(C) gene; 4: 186 bp DNA fragment of DocA gene. (b2) M: marker DL2000; 1: 957 bp DNA fragment of fusion eYFP(N)-Coh gene; 2: 456 bp DNA fragment of Coh gene; 3: 474 bp DNA fragment of fusion DocA-D1-eYFP(C) gene; 4: 186 bp DNA fragment of DocA-D1 gene. (b3) M: marker DL2000; 1: 957 bp DNA fragment of fusion eYFP(N)-Coh gene; 2: 456 bp DNA fragment of Coh gene; 3: 474 bp DNA fragment of fusion DocA-D2-eYFP(C) gene; 4: 186 bp DNA fragment of DocA-D2 gene. (b4) M: marker DL2000; 1: 957 bp DNA fragment of fusion eYFP(N)-Coh gene; 2: 456 bp DNA fragment of Coh gene; 3: 474 bp DNA fragment of fusion DocA-D3-eYFP(C) gene; 4: 186 bp DNA fragment of DocA-D3 gene. (b5) M: marker DL2000; 1: 957 bp DNA fragment of fusion eYFP(N)-Coh gene; 2: 456 bp DNA fragment of Coh gene; 3: 474 bp DNA fragment of fusion DocA-D4-eYFP(C) gene; 4: 186 bp DNA fragment of DocA-D4 gene. (b6) M: marker DL2000; 1: 930 bp DNA fragment of fusion eYFP(N)-SpyCatcher gene; 2: 423 bp DNA fragment of SpyCatcher gene; 3: 330 bp DNA fragment of fusion SpyTag-eYFP(C) gene; 4: 39 bp DNA fragment of SpyTag gene. (**C**) Fluorescence signal intensity changes in eYFP-DocA mutants/Coh expressed via BiFC-FC fusion. (**D**) Median value of fluorescence signal intensity of eYFP-DocA mutants/Coh.

3.6. MD Simulation and Structural Analysis of DocA Mutants

For the four DocA mutants, different DocA–Coh complexes were constructed using PyMOL 2.3.2 and then GROMACS 4.5 software was used to perform a 10 ns MD simulation in explicit water. The changes in the simulated structure of the mutant protein under a GROMOS 96 force field are shown in Figure 4. The detailed analysis and comparison of the MD simulation showed that the mutant protein body and the original protein had a large or a small gap, and the changes were mainly concentrated in the loop section. According to the comparative analysis, as shown in Figure 4(A1,A2), in the presence of Ca^{2+}, the α1 and α3 helices of the original DocA existed stably at a fixed angle; without Ca^{2+}, the α1 and α3 helices were looser and the displacement was obvious. The comparative analysis of the mutant proteins is shown in Figure 4(B1–B4). The α1 and α3 helices of mutant DocA-D3 and DocA-D4 could form a stable bond with Coh at a certain angle (without Ca^{2+}). For the changes in the amino acid position (Figures 4 and S3), the mutation of Asp9 of the original DocA to Ser9 made the loop region of the calcium-binding site more compact, as observed with the mutants DocA-D2, DocA-D3, and DocA-D4; among them, DocA-D3 combined the two mutations on Asp7 and Arg11, which made the interaction with Coh more stable.

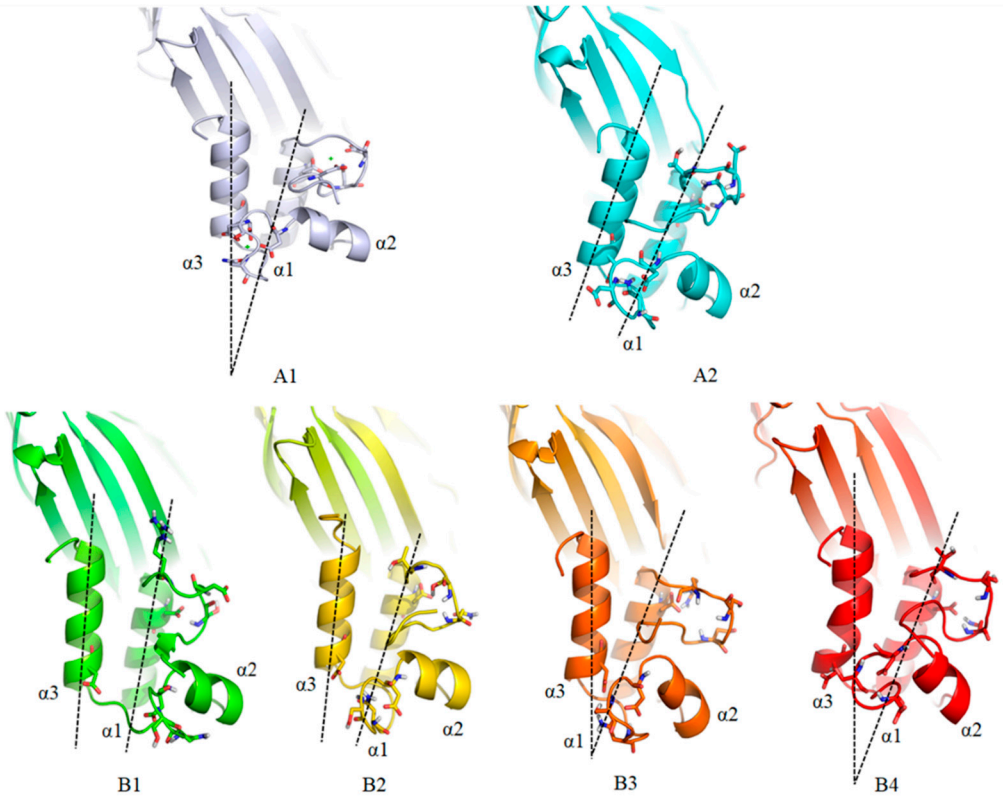

Figure 4. Comparison of DocA mutants and Coh simulation structures. (**A1**) The structure of original DocA and Coh in the presence of Ca^{2+}. (**A2**) The structure of original DocA and Coh in the absence Ca^{2+}. (**B1**) The structure of DocA-D1 and Coh in the absence of Ca^{2+}. (**B2**) The structure of DocA-D2 and Coh in the absence of Ca^{2+}. (**B3**) The structure of DocA-D3 and Coh in the absence of Ca^{2+}. (**B4**) The structure of DocA-D4 and Coh in the absence of Ca^{2+}.

Using the g_rms tool in the Gromacs 4.5 software, we analyzed the different parameters (RMSD) between the mutant structure and the wild-type DocA structure (with/without Ca^{2+}) and plotted them onto a scatter plot, as shown in Figure 5A,B. The results showed that the RMSD data of mutants DocA-D3 and DocA-D4 were lower than the RMSD data of the original DocA (without Ca^{2+}), i.e., the structure of DocA-D3 and DocA-D4 was more stable than that of DocA (without Ca^{2+}). To further evaluate the structural similarity of the four mutants to DocA, the frequency counts of the RMSD values of the mutants

were calculated, as shown in Figure 5C,D. In the 10 ns simulation, in the absence of Ca^{2+}, the DocA structure was extremely unstable, and the RMSD frequency was the highest (0.35). The mutants (without Ca^{2+}) tended to be stable, and the highest RMSD frequency of DocA-D3 and DocA-D4 was 0.29, which was even lower than the theoretical most stable state value without a mutation (0.31). The highest RMSD frequency of the interaction between Coh and DocA-D3 was slightly high, reaching 0.21, indicating that this section of Coh needed to undergo further changes to adapt to the stabilizing effect of the mutant.

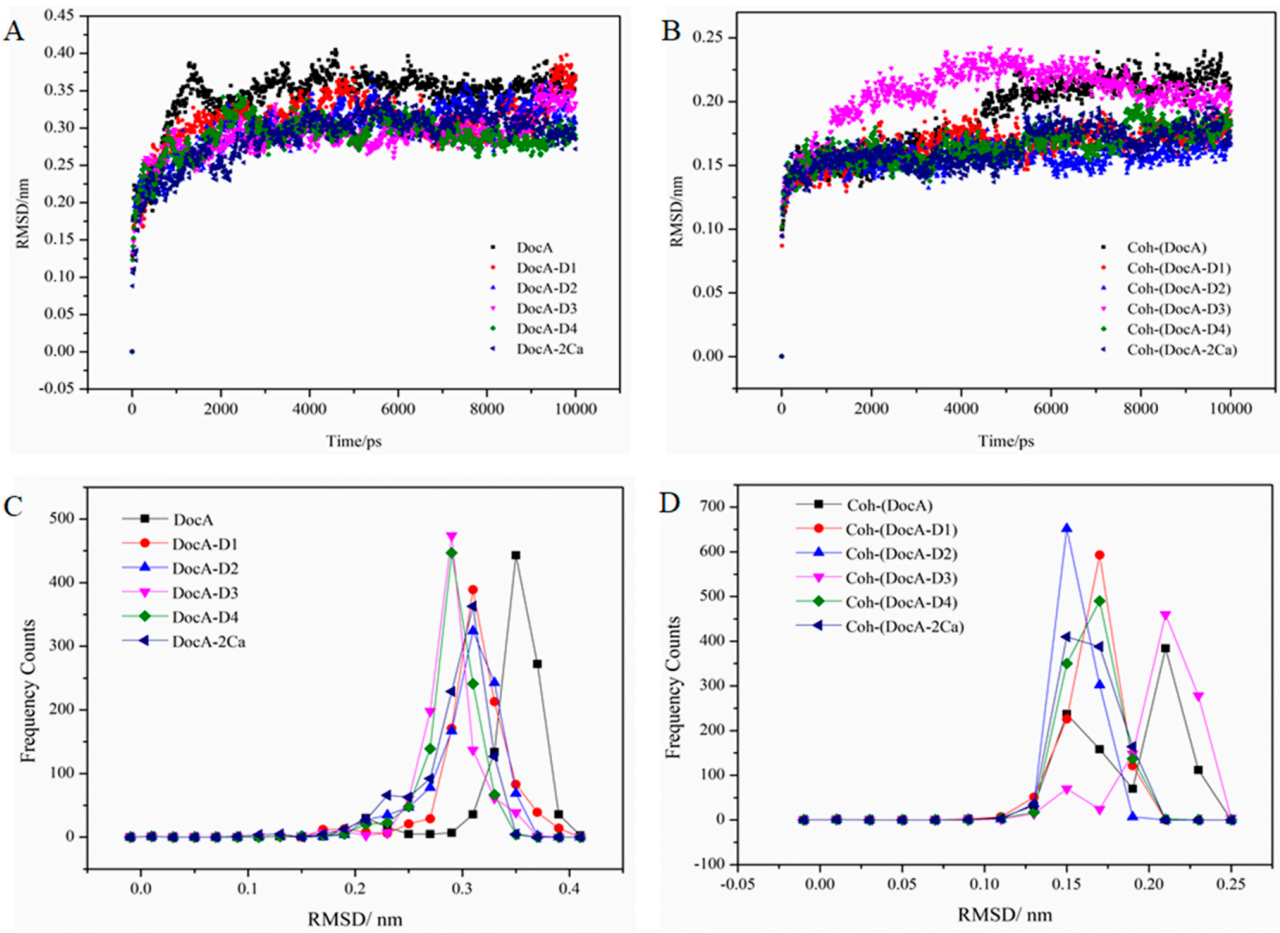

Figure 5. RMSD scatter plots of DocA mutants/Coh in molecular dynamics simulation. (**A**) Scatter plots of RMSD values of DocA mutants. (**B**) Scatter plots of the RMSD value of Coh interacting with the DocA mutants. (**C**) The total frequency chart of the RMSD value of the DocA mutants. (**D**) The total frequency chart of the RMSD value of Coh interacting with DocA mutants.

3.7. Efficient Assembly and Detection of Key Enzymes for L-Lysine Production

AspC and LysC are the two initial key enzymes in the L-lysine synthesis pathway. They were assembled using the cellulosome complex model to optimize the fermentation efficiency of the strain. After the above-mentioned in vitro and in vivo interaction experiments and MD simulations, the mutant DocA-D3 was selected as the optimal mutant. In the absence of Ca^{2+} in the cell, it could stably interact with Coh. The fermentation result of the intracellular cellulosomes element assembly complex is shown in Figure 6A. During 8–24 h of fermentation, the OD_{600} value of the assembled engineering bacteria *E. coli* QDE-DocA-D3 increased rapidly, which was 2.2–3.4 times that of *E. coli* QDE. At the same time, as shown in Figure 6B, when the amount of residual sugar was ensured, the carbon source was quickly consumed at this stage, and the efficiency of L-lysine synthesis was significantly improved. At the end of the fermentation, the concentration of L-lysine

obtained from the assembly engineering strain QDE-DocA-D3 accumulated to 60.3 g/L, which was 24.1% higher than that of the starting strain QDE.

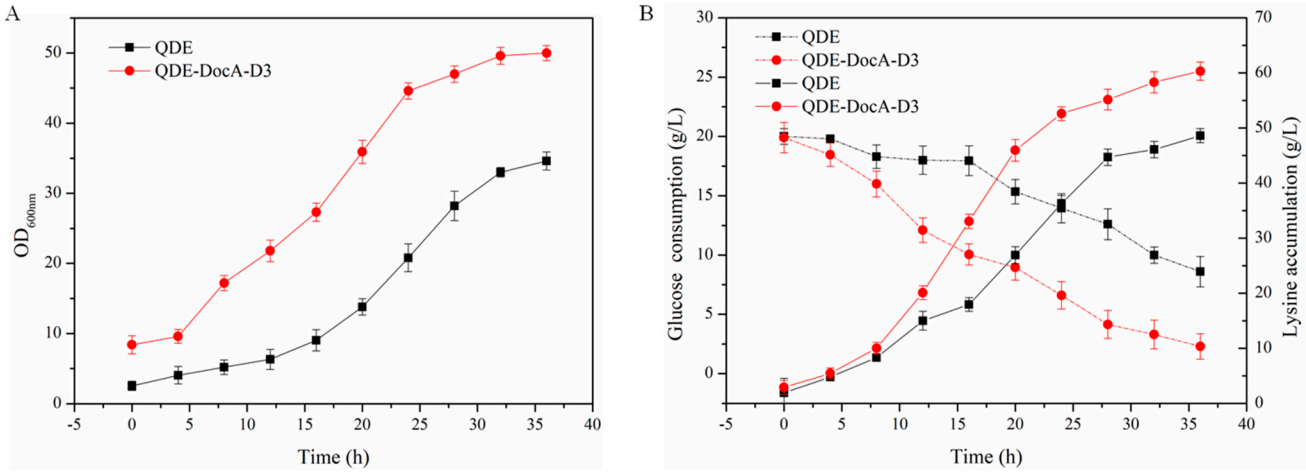

Figure 6. Assembly efficiency of cellulosome elements combined with key enzymes in L-lysine fermentation. (**A**) The changes in OD_{600} during fermentation and growth of bacterial cells. (**B**) The changes in carbon source consumption and L-lysine accumulation during bacterial growth and fermentation.

3.8. Efficient Assembly and Detection of Key Enzymes for β-Alanine Production

β-Alanine was prepared through enzymatic conversion by the double-enzymatic coupling of AspA and PanD. The reaction conditions were mild, and the conversion rate was high. Using sodium glutamate and oxaloacetate as substrates, the intermediate product L-aspartic acid was accumulated by the action of AspA, and β-alanine was synthesized under the further action of PanD. DocA-D3 and Coh were co-expressed with two key enzymes, AspA and PanD, respectively, for assembly and fermentation in *E. coli* cells. Through the intraregional interaction of DocA-D3 and Coh, the efficiency of both AspA and PanD enzymes was promoted. The results of intracellular assembly and fermentation of the engineered strain *E. coli* QD01-DocA-D3-Ala are shown in Figure 7. Within 0–8 h, the β-alanine accumulation of the assembled engineered bacteria *E. coli* QD01-DocA-D3-Ala and the starting bacteria *E. coli* QD01 increased simultaneously. During the 8–22 h fermentation, the yield from *E. coli* QD01 increased to 7.51 g/L, while that from *E. coli* QD01-DocA-D3-Ala increased rapidly to 18.65 g/L, which was a 2.48-fold increase. This indicated that the intracellular assembly of the key cellulosome components DocA-D3/Coh brought the key enzymes closer together and promoted fermentation efficiency. During the 22–30 h fermentation, the β-alanine accumulation of *E. coli* QD01-DocA-D3-Ala strain could be maintained at a high level, which was 2.13–2.63 times that of *E. coli* QD01, and the synthesis efficiency was significantly improved.

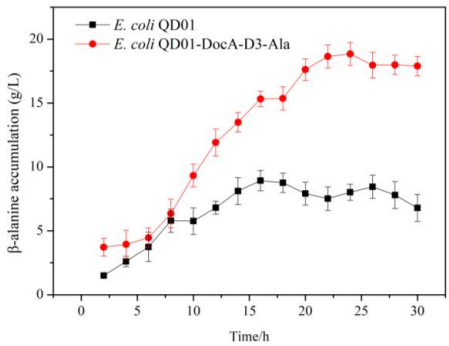

Figure 7. Assembly efficiency of cellulosome elements combined with key enzymes in β-alanine fermentation. Changes in β-alanine accumulation during bacterial fermentation.

Through the above verification, it was evident that the use of DocA-D3 components significantly improved the fermentation efficiency of the production strains. Thus, DocA-D3 could be used to assemble intracellular cellulosomes, shorten the working distance and time, and improve the synthesis efficiency.

4. Conclusions

A novel design method was used to directionally modify the Ca^{2+}-binding site of the key components of cellulosome, and four double-site DocA mutants were obtained. At a Ca^{2+} concentration between 10^{-7} and 10^{-4} M, DocA-D3 had the strongest binding affinity, which was 8.01 times that of DocA. The self-assembly fluorescence intensity of the four mutants in *E. coli* reached up to 1.26×10^7, indicating that they could interact with Coh in vivo. Moreover, DocA-D3 was applied to the intracellular assembly of key enzymes in L-lysine and β-alanine fermentation, laying the foundation for improving the efficiency of intracellular assembly and fermentation.

Supplementary Materials: The following supporting information can be downloaded at: https://www.mdpi.com/article/10.3390/fermentation8110578/s1, Figure S1: The construction and schematic representation of the recombinant plasmids; Figure S2: Electrophoretogram of purified proteins; Figure S3: Changes in the key amino acid positions of DocA mutants; Table S1: The list of verification primers in this study. Introduced restriction sites (RS) are underlined.

Author Contributions: Conceptualization, N.L. and J.W.; methodology, N.L.; software, J.W.; validation, N.L., L.X. and Z.W.; formal analysis, P.D.; investigation, J.S.; resources, J.X.; data curation, P.L.; writing—original draft preparation, N.L.; writing—review and editing, L.X.; visualization, Z.W.; supervision, J.W.; project administration, M.W.; funding acquisition, R.W. All authors have read and agreed to the published version of the manuscript.

Funding: This work was supported by the National Science Foundation of China (31801527), Focus on Research and Development Plan in Shandong Province (2021ZDSYS10, 2020CXGC010603, 2019JZZY011003), Taishan industry leading talent (tscy20180103), National Key Research and Development Project (2019YFC1905900), Cultivation Project of Shandong Synthetic Biotechnology Innovation Center (sdsynbio-2018-PY-02) and Qilu University of Technology (Shandong Academy of Sciences) "open competition mechanism" project (2022JBZ01-06).

Institutional Review Board Statement: Not applicable.

Informed Consent Statement: Not applicable.

Data Availability Statement: Not applicable.

Conflicts of Interest: The authors declare no conflict of interest.

References

1. Liu, C.K.; Pedley, A.M.; He, J.X.; Johnson, J.L.; Yaron, T.M.; Cantley, L.C.; Benkovic, S.J. Biocatalytic cascades operating on macromolecular scaffolds and in confined environments. *Nat. Catal.* **2020**, *3*, 256–273.
2. Fletcher, J.M.; Harniman, R.L.; Barnes, F.R.H.; Boyle, A.L.; Collins, A.; Mantell, J.; Sharp, T.H.; Antognozzi, M.; Booth, P.J.; Linden, N.; et al. Self-assembling cages from coiled-coil peptide modules. *Science* **2013**, *340*, 595–599. [CrossRef]
3. Nakase, I.; Okumura, S.; Tanaka, G.; Osaki, K.; Imanishi, M.; Futaki, S. Signal transduction using an artificial receptor system that undergoes dimerization upon addition of a bivalent leucine-zipper ligand. *Angew. Chem. Int. Ed.* **2012**, *51*, 7464–7467. [CrossRef]
4. Thomas, F.; Boyle, A.L.; Burton, A.J.; Woolfson, D.N. A set of de novo designed parallel heterodimeric coiled coils with quantified dissociation constants in the micromolar to sub-nanomolar regime. *J. Am. Chem. Soc.* **2013**, *135*, 5161–5166. [CrossRef] [PubMed]
5. Lee, M.J.; Brown, I.R.; Juodeikis, R.; Frank, S.; Warren, M.J. Employing bacterial microcompartment technology to engineer a shell-free enzyme-aggregate for enhanced 1,2-propanediol production in *Escherichia coli*. *Metab. Eng.* **2016**, *36*, 48–56. [CrossRef] [PubMed]
6. Wang, Y.; Leng, L.; Islam, M.K.; Liu, F.; Lin, C.S.; Leu, S.Y. Substrate-related factors affecting cellulosome-induced hydrolysis for lignocellulose valorization. *Int. J. Mol. Sci.* **2019**, *20*, 3354. [CrossRef]
7. Hirano, K.; Kurosaki, M.; Nihei, S.; Hasegawa, H.; Shinoda, S.; Haruki, M.; Hirano, N. Enzymatic diversity of the *Clostridium thermocellum* cellulosome is crucial for the degradation of crystalline cellulose and plant biomass. *Sci. Rep.* **2016**, *6*, 35709. [CrossRef]

8. Fontes, C.; Gilbert, H.J. Cellulosomes: Highly efficient nanomachines designed to deconstruct plant cell wall complex carbohydrates. *Annu. Rev. Biochem.* **2010**, *79*, 655–681. [CrossRef]
9. Barth, A.; Hendrix, J.; Fried, D.; Barak, Y.; Bayer, E.A.; Lamb, D.C. Dynamic interactions of type I cohesin modules fine-tune the structure of the cellulosome of *Clostridium thermocellum*. *Proc. Natl. Acad. Sci. USA* **2018**, *115*, 11274–11283. [CrossRef]
10. Fan, L.H.; Zhang, Z.J.; Yu, X.Y.; Xue, Y.X.; Tan, T.W. Self-surface assembly of cellulosomes with two miniscaffoldins on *Saccharomyces cerevisiae* for cellulosic ethanol production. *Proc. Natl. Acad. Sci. USA* **2012**, *109*, 13260–13265. [CrossRef]
11. Fan, L.H.; Zhang, Z.J.; Yu, X.Y.; Xue, Y.X.; Wang, M.M.; Tan, T.W. In vitro assembly of minicellulosomes with two scaffoldins on the yeast cell surface for cellulose saccharification and bioethanol production. *Process Biochem.* **2013**, *48*, 430–437. [CrossRef]
12. Kostas, T.; Sylvie, S.; Pierre, B. Interaction of the duplicated segment carried by *Clostridium thermocellum* cellulases with cellulosome components. *FEBS Lett.* **1991**, *291*, 185–188.
13. Chen, C.; Yang, H.W.; Xuan, J.S. Resonance assignments of a cellulosomal double-dockerin from *Clostridium thermocellum*. *Biomol. NMR Assign.* **2019**, *13*, 97–101. [CrossRef] [PubMed]
14. Carvalho, A.L.; Dias, F.; Prates, J.; Nagy, T.; Gilbert, H.J.; Davies, G.J.; Ferreira, L.; Romao, M.J.; Fontes, C. Cellulosome assembly revealed by the crystal structure of the cohesin-dockerin complex. *Proc. Natl. Acad. Sci. USA* **2003**, *100*, 13809–13814. [CrossRef]
15. Betsy, L.L.; Brian, F.V.; William, M.W. Secondary structure and calcium-induced folding of the *Clostridium thermocellum* dockerin domain determined by NMR spectroscopy. *Arch. Biochem. Biophys.* **2000**, *379*, 237–244.
16. Choi, S.K.; Ljungdah, L.G. Structural role of calcium for the organization of the cellulosome of *Clostridium thermocellum*. *Biochemistry* **1996**, *35*, 4906–4910. [CrossRef]
17. Bule, P.; Cameron, K.; Prates, J.A.M.; Ferreira, L.M.A.; Smith, S.P.; Gilbert, H.J.; Bayer, E.A.; Najmudin, S.; Fontes, C.M.G.A.; Alves, V.D. Structure-function analyses generate novel specificities to assemble the components of multienzyme bacterial cellulosome complexes. *J. Biol. Chem.* **2018**, *293*, 4201–4212. [CrossRef] [PubMed]
18. Xu, Q.; Ding, S.Y.; Brunecky, R.; Bomble, Y.J.; Himmel, M.E.; Baker, J.O. Improving activity of minicellulosomes by integration of intra- and intermolecular synergies. *Biotechnol. Biofuels* **2013**, *6*, 126. [CrossRef]
19. Lim, H.J.; Sode, K.; Tamiya, E.; Karube, I.J.M. Enzymatic hydrolysis of cristalline cellulose in organic solvent. *Metallomics* **2011**, *3*, 656–661.
20. Carvalho, A.L.; Dias, F.; Nagy, T.; Prates, J.; Proctor, M.R.; Smith, N.; Bayer, E.A.; Davies, G.J.; Ferreira, L.; Romao, M.J. Evidence for a dual binding mode of dockerin modules to cohesins. *Proc. Natl. Acad. Sci. USA* **2007**, *104*, 3089–3094. [CrossRef]
21. Irina, G.; Margarita, M.; Elena, Z. New Kunitz-type HCRG polypeptides from the sea anemone *Heteractis crispa*. *Mar. Drugs* **2015**, *13*, 6038–6063.
22. Morell, M.; Czihal, P.; Hoffmann, R.; Otvos, L.; Aviles, F.X.; Ventura, S. Monitoring the interference of protein-protein interactions in vivo by bimolecular fluorescence complementation: The DnaK case. *Proteomics* **2008**, *8*, 3433–3442. [CrossRef] [PubMed]
23. Morell, M.; Espargaro, A.; Aviles, F.X.; Ventura, S. Detection of transient protein-protein interactions by bimolecular fluorescence complementation: The Abl-SH3 case. *Proteomics* **2007**, *7*, 1023–1036. [CrossRef]
24. Parvatiyar, K.; Zhang, Z.; Teles, R.M.; Ouyang, S.; Jiang, Y.; Iyer, S.S.; Zaver, S.A.; Schenk, M.; Zeng, S.; Zhong, W.; et al. The helicase DDX41 recognizes the bacterial secondary messengers cyclic di-GMP and cyclic di-AMP to activate a type I interferon immune response. *Nat. Immunol.* **2012**, *13*, 1155–1161. [CrossRef]
25. Wang, J.; Ren, X.; Wang, R.; Su, J.; Wang, F. Structural characteristics and function of a new kind of thermostable trehalose synthase from *Thermobaculum terrenum*. *J. Agric. Food Chem.* **2017**, *65*, 7726–7735. [CrossRef]
26. Xu, J.; Han, M.; Ren, X. Modification of aspartokinase III and dihydrodipicolinate synthetase increases the production of L-lysine in *Escherichia coli*. *Biochem. Eng. J.* **2016**, *114*, 79–86. [CrossRef]
27. Chowdhury, C.; Sinha, S.; Chun, S.; Yeates, T.O.; Bobik, T.A. Diverse bacterial microcompartment organelles. *Proc. Natl. Acad. Sci. USA* **2014**, *78*, 438–468. [CrossRef] [PubMed]
28. Lehman, B.P.; Chowdhury, C.; Bobik, T.A. The N terminus of the PduB protein binds the protein shell of the Pdu microcompartment to its enzymatic core. *J. Bacteriol.* **2017**, *199*, e00785-16. [CrossRef]
29. Yang, M.; Simpson, D.M.; Wenner, N.; Brownridge, P.; Harman, V.M.; Hinton, J.C.D.; Beynon, R.J.; Liu, L.N. Decoding the stoichiometric composition and organisation of bacterial metabolosomes. *Nat. Commun.* **2020**, *11*, 1976. [CrossRef]
30. Kerfeld, C.A.; Melnicki, M.R. Assembly, function and evolution of cyanobacterial carboxysomes. *Curr. Opin. Plant Biol.* **2016**, *31*, 66–75. [CrossRef]
31. Rae, B.D.; Long, B.M.; Badger, M.R.; Price, G.D. Functions, compositions, and evolution of the two types of carboxysomes: Polyhedral microcompartments that facilitate CO_2 fixation in cyanobacteria and some proteobacteria. *Microbiol. Mol. Biol. Rev.* **2013**, *77*, 357–379. [CrossRef]
32. Amelung, S.; Nerlich, A.; Rohde, M.; Spellerberg, B.; Cole, J.N.; Nizet, V.; Chhatwal, G.S.; Talay, S.R. The FbaB-type fibronectin-binding protein of *Streptococcus pyogenes* promotes specific invasion into endothelial cells. *Cell. Microbiol.* **2011**, *13*, 1200–1211. [CrossRef] [PubMed]
33. Hagan, R.M.; Bjornsson, R.; McMahon, S.A.; Schomburg, B.; Braithwaite, V.; Buhl, M.; Naismith, J.H.; Schwarz-Linek, U. NMR spectroscopic and theoretical analysis of a spontaneously formed Lys-Asp isopeptide bond. *Angew. Chem. Int. Ed.* **2010**, *49*, 8421–8425. [CrossRef] [PubMed]
34. Zakeri, B.; Fierer, J.O.; Celik, E.; Chittock, E.C.; Schwarz-Linek, U.; Moy, V.T.; Howarth, M. Peptide tag forming a rapid covalent bond to a protein, through engineering a bacterial adhesin. *Proc. Natl. Acad. Sci. USA* **2012**, *109*, E690–E697. [CrossRef] [PubMed]

35. Brune, K.D.; Leneghan, D.B.; Brian, I.J.; Ishizuka, A.S.; Bachmann, M.F.; Draper, S.J.; Biswas, S.; Howarth, M. Plug-and-display: Decoration of virus-like particles via isopeptide bonds for modular immunization. *Sci. Rep.* **2016**, *6*, 19234. [CrossRef]
36. Chen, A.Y.; Deng, Z.T.; Billings, A.N.; Seker, U.O.S.; Lu, M.Y.; Citorik, R.J.; Zakeri, B.; Lu, T.K. Synthesis and patterning of tunable multiscale materials with engineered cells. *Nat. Mater.* **2014**, *13*, 515–523. [CrossRef]
37. Veggiani, G.; Zakeri, B.; Howarth, M. Superglue from bacteria: Unbreakable bridges for protein nanotechnology. *Trends Biotechnol.* **2014**, *32*, 506–512. [CrossRef]
38. Wang, J.; Wang, Y.; Wang, X.; Zhang, D.; Wu, S.; Zhang, G. Enhanced thermal stability of lichenase from *Bacillus subtilis* 168 by SpyTag/SpyCatcher-mediated spontaneous cyclization. *Biotechnol. Biofuels* **2016**, *9*, 79. [CrossRef]
39. Chowdhury, C.; Chun, S.; Pang, A.; Sawaya, M.R.; Sinha, S.; Yeates, T.O.; Bobik, T.A. Selective molecular transport through the protein shell of a bacterial microcompartment organelle. *Proc. Natl. Acad. Sci. USA* **2015**, *112*, 2990–2995. [CrossRef]
40. Kennedy, N.W.; Ikonomova, S.P.; Lee, M.S.; Raeder, H.W.; Tullman-Ercek, D. Self-assembling shell proteins PduA and PduJ have essential and redundant roles in bacterial microcompartment assembly. *J. Mol. Biol.* **2021**, *433*, 166721. [CrossRef]
41. Pang, A.; Liang, M.; Prentice, M.B.; Pickersgill, R.W. Substrate channels revealed in the trimeric *Lactobacillus reuteri* bacterial microcompartment shell protein PduB. *Acta Crystallogr.* **2012**, *68*, 1642–1652.
42. Lee, M.J.; Mantell, J.; Hodgson, L.; Alibhai, D.; Fletcher, J.M.; Brown, I.R.; Frank, S.; Xue, W.F.; Verkade, P.; Woolfson, D.N.; et al. Engineered synthetic scaffolds for organizing proteins within the bacterial cytoplasm. *Nat. Chem. Biol.* **2018**, *14*, 142–147. [CrossRef] [PubMed]
43. Young, E.J.; Burton, R.; Mahalik, J.P.; Sumpter, B.G.; Fuentes-Cabrera, M.; Kerfeld, C.A.; Ducat, D.C. Engineering the bacterial microcompartment domain for molecular scaffolding applications. *Front. Microbiol.* **2017**, *8*, 1441. [CrossRef] [PubMed]
44. Vita, N.; Borne, R.; Fierobe, H.P. Cell-surface exposure of a hybrid 3-cohesin scaffoldin allowing the functionalization of *Escherichia coli* envelope. *Biotechnol. Bioeng.* **2020**, *117*, 626–636. [CrossRef] [PubMed]
45. Tsai, S.L.; Oh, J.; Singh, S.; Chen, R.; Chen, W. Functional assembly of minicellulosomes on the *Saccharomyces cerevisiae* cell surface for cellulose hydrolysis and ethanol production. *Appl. Environ. Microbiol.* **2009**, *75*, 6087–6093. [CrossRef]
46. Fierobe, H.P.; Bayer, E.A.; Tardif, C.; Czjzek, M.; Mechaly, A.; Bélaïch, A.; Lamed, R.; Shoham, Y.; Bélaïch, J.P. Degradation of cellulose substrates by cellulosome chimeras: Substrate targeting versus proximity of enzyme components. *J. Biol. Chem.* **2002**, *277*, 49621–49630. [CrossRef]
47. Fierobe, H.P.; Mingardon, F.; Mechaly, A.; Bélaïch, A.; Rincon, M.T.; Pagès, S.; Lamed, R.; Tardif, C.; Bélaïch, J.P.; Bayer, E.A. Action of designer cellulosomes on homogeneous versus complex substrates-controlled incorporation of three distinct enzymes into a defined trifunctional scaffoldin. *J. Biol. Chem.* **2005**, *280*, 16325–16334. [CrossRef]
48. Bae, J.; Kuroda, K.; Ueda, M. Proximity effect among cellulose-degrading enzymes displayed on the *Saccharomyces cerevisiae* cell surface. *Appl. Environ. Microbiol.* **2015**, *81*, 59–66. [CrossRef]
49. Arsov, A.; Petrov, K.; Petrova, P. Enhanced activity by genetic complementarity: Heterologous secretion of clostridial cellulases by *Bacillus licheniformis* and *Bacillus velezensis*. *Molecules* **2021**, *26*, 5625. [CrossRef]
50. Anandharaj, M.; Lin, Y.J.; Rani, R.P.; Nadendla, E.K.; Ho, M.C.; Huang, C.C.; Cheng, J.F.; Chang, J.J.; Li, W.H. Constructing a yeast to express the largest cellulosome complex on the cell surface. *Proc. Natl. Acad. Sci. USA* **2020**, *117*, 2385–2394. [CrossRef]
51. Bule, P.; Alves, V.D.; Leitao, A.; Ferreira, L.M.A.; Bayer, E.A.; Smith, S.P.; Gilbert, H.J.; Najmudin, S.; Fontes, C. Single binding mode integration of hemicellulose-degrading enzymes via adaptor scaffoldins in *Ruminococcus flavefaciens* cellulosome. *J. Biol. Chem.* **2016**, *291*, 26658–26669. [CrossRef]
52. Jeon, S.D.; Lee, J.E.; Kim, S.J.; Kim, S.W.; Han, S.O. Analysis of selective, high protein-protein binding interaction of cohesin-dockerin complex using biosensing methods. *Biosens. Bioelectron.* **2012**, *35*, 382–389. [CrossRef] [PubMed]
53. Liang, Y.Y.; Si, T.; Ang, E.L.; Zhao, H.M. Engineered pentafunctional minicellulosome for simultaneous saccharification and ethanol fermentation in *Saccharomyces cerevisiae*. *Appl. Environ. Microbiol.* **2014**, *80*, 6677–6684. [CrossRef]
54. Grinberg, I.R.; Yaniv, O.; de Ora, L.O.; Muñoz-Gutiérrez, I.; Hershko, A.; Livnah, O.; Bayer, E.A.; Borovok, I.; Frolow, F.; Lamed, R.; et al. Distinctive ligand-binding specificities of tandem PA14 biomass-sensory elements from *Clostridium thermocellum* and *Clostridium clariflavum*. *Proteins Struct. Funct. Bioinform.* **2019**, *87*, 917–930. [CrossRef] [PubMed]
55. Gunnoo, M.; Cazade, P.-A.; Orlowski, A.; Chwastyk, M.; Liu, H.; Ta, D.T.; Cieplak, M.; Nash, M.; Thompson, D. Steered molecular dynamics simulations reveal the role of Ca^{2+} in regulating mechanostability of cellulose-binding proteins. *Phys. Chem. Chem. Phys.* **2018**, *20*, 22674–22680. [CrossRef]
56. Case, D.A.; Iii, T.; Darden, T.; Gohlke, H.; Luo, R.; Merz, K.M.; Onufriev, A.; Simmerling, C.; Wang, B.; Woods, R.J. The Amber biomolecular simulation programs. *J. Comput. Chem.* **2010**, *26*, 1668–1688. [CrossRef] [PubMed]